IMPLEMENTATION AND VALIDATION OF EULER SOLVERS FOR LAUNCH VEHICLE FLOWS

J. L. F. Azevedo†, F. Zdravistch*, and A. F. C. Silva‡
†Instituto de Aeronáutica e Espaço, Centro Técnico Aeroespacial, 12225 – São José dos Campos – SP – Brazil
*Instituto Tecnológico de Aeronáutica, Centro Técnico Aeroespacial, 12225 – São José dos Campos – SP – Brazil
‡Departamento Engenharia Mecânica, Universidade Federal de Santa Catarina, 88049 – Florianópolis – SC – Brazil

ABSTRACT

The development of a three dimensional, finite difference, Euler solver is presented, and aspects of its validation are discussed. The Beam and Warming implicit approximate factorization algorithm is used for the numerical solution of the governing equations. Applications consider the aerodynamic design of general satellite launch vehicles with a single body configuration. Since no experimental results were available for the configuration of interest, major emphasis in the validation of the present code was placed upon comparison with zero angle of attack results given by a previously validated axisymmetric code. The present calculations are shown to be within acceptable accuracy limits, for the region of interest, to be used in preliminary design applications.

INTRODUCTION

The development of a satellite launcher is an undertaking that requires considerable maturity and commitment of any country aerospace community. The development of the first Brazilian satellite launcher, the VLS, has been going on for a few years, and the present effort is undertaken in the context of such work. Moreover, in a project of such dimensions, many other smaller, or special purpose vehicles may have to be built in order to test some subsystems of the launcher itself. Considering that wind tunnel tests can be quite expensive, especially because they have to be performed overseas in our case, it is important to develop the capability of computing these aerodynamic flowfields. In particular, the present work arose from the need to obtain accurate aerodynamic data for one of these special purpose vehicles. Detailed pressure distributions at the vehicle's nose fairing, at angle of attack, were required in order to structurally design the fairing to withstand the internal-external pressure imbalance. Due to project cost limitations, the only available means to obtain this data was through computation.

The work describes, then, the efforts in terms of development and validation of Euler solvers that can be used for the aerodynamic design of satellite launch vehicles. The reason for working with an inviscid formulation is primarily a question of implementation simplicity associated to the fact that we are, initially, only interested in body pressure distributions. The governing equations are written in conservation-law form for 3-D, body-conforming, general curvilinear coordinates. The Beam and Warming implicit approximate factorization algorithm[1, 2] is used to discretize and solve the resulting finite difference equations in delta form.

An important aspect of the present work concerns the validation of the computations here performed. Since no experimental pressure distributions over the vehicle of interest were available, other means of validation had to be used. In this case, the major emphasis in this validation effort was in the comparison of the three dimensional computations for zero angle of attack with those obtained with an axisymmetric Euler solver previously developed by some of the present authors[3, 4]. The axisymmetric code had previously been validated against experimental results[5] available for the VLS vehicle itself. In the following sections, the theoretical formulation of the problem is presented and details of the numerical implementation are discussed. The computational results obtained in the present investigation are presented together with comparisons with available data. Finally, the sensitivity of the present solutions to various computational parameters, such as grid refinement and magnitude of artificial dissipation terms, is investigated using primarily the axisymmetric code.

THEORETICAL BACKGROUND

The compressible Euler equations can be written in strong conservation-law form for general three dimensional, body-conforming, curvilinear coordinates as

$$\frac{\partial \overline{Q}}{\partial \tau} + \frac{\partial \overline{E}}{\partial \xi} + \frac{\partial \overline{F}}{\partial \eta} + \frac{\partial \overline{G}}{\partial \zeta} = 0 \tag{1}$$

where the vector of conserved quantities, $\overline{Q}$, is defined as

$$\overline{Q} = J^{-1}\left[\rho\ ,\ \rho u\ ,\ \rho v\ ,\ \rho w\ ,\ e\right]^T \tag{2}$$

The flux vectors $\overline{E}$, $\overline{F}$ and $\overline{G}$ can be written as

$$\overline{E} = J^{-1}\begin{Bmatrix} \rho U \\ \rho u U + p\xi_x \\ \rho v U + p\xi_y \\ \rho w U + p\xi_z \\ (e+p)U - p\xi_t \end{Bmatrix} \qquad \overline{F} = J^{-1}\begin{Bmatrix} \rho V \\ \rho u V + p\eta_x \\ \rho v V + p\eta_y \\ \rho w V + p\eta_z \\ (e+p)V - p\eta_t \end{Bmatrix} \qquad \overline{G} = J^{-1}\begin{Bmatrix} \rho W \\ \rho u W + p\zeta_x \\ \rho v W + p\zeta_y \\ \rho w W + p\zeta_z \\ (e+p)W - p\zeta_t \end{Bmatrix} \tag{3}$$

In the above equations, the usual nomenclature is being used. Therefore, ρ is the density, u, v and w are the cartesian components of velocity, and e is the total energy per unit of volume. The equations have been nondimensionalized following the work of Pulliam and Steger[6, 7].

The pressure, p, can be obtained by the equation of state for perfect gases

$$p = (\gamma - 1)\rho e_i = (\gamma - 1)\left[e - \frac{1}{2}\rho\left(u^2 + v^2 + w^2\right)\right] \tag{4}$$

where e_i is the specific internal energy of the fluid, and γ is the ratio of specific heats. The contravariant velocity components are defined as

$$U = \xi_t + \xi_x u + \xi_y v + \xi_z w \qquad V = \eta_t + \eta_x u + \eta_y v + \eta_z w \qquad W = \zeta_t + \zeta_x u + \zeta_y v + \zeta_z w \tag{5}$$

Throughout this work, the curvilinear coordinate system is defined such that ξ is the longitudinal direction, η is the normal direction, and ζ is the circumferential direction. This coordinate system is obtained from the transformation of variables

$$\tau = t \qquad \xi = \xi(x, y, z, t) \qquad \eta = \eta(x, y, z, t) \qquad \zeta = \zeta(x, y, z, t) \tag{6}$$

Expressions for the Jacobian of the transformation, J, and for the various metric relations can be found in Pulliam and Steger[6, 7], and Azevedo[8].

Details of the axisymmetric formulation are presented by Zdravistch[3], and Zdravistch and Azevedo[4]. The formulation implemented is actually very similar to the one presented by Nietubicz et al.[9]. This is actually an azimuthal invariant formulation, in which the Euler equations can be rewritten as

$$\frac{\partial \tilde{Q}}{\partial \tau} + \frac{\partial \tilde{E}}{\partial \xi} + \frac{\partial \tilde{F}}{\partial \eta} + \tilde{H} = 0 \tag{7}$$

The vector of conserved variables $\tilde{Q}$ is given by

$$\tilde{Q} = J^{-1}\left[\rho\ ,\ \rho u\ ,\ \rho v\ ,\ e\right]^T \tag{8}$$

The flux vectors $\tilde{E}$ and $\tilde{F}$, and the source term $\tilde{H}$ can be written as

$$\tilde{E} = J^{-1}\begin{Bmatrix} \rho U \\ \rho u U + p\xi_x \\ \rho v U + p\xi_y \\ (e+p)U - p\xi_t \end{Bmatrix} \qquad \tilde{F} = J^{-1}\begin{Bmatrix} \rho V \\ \rho u V + p\eta_x \\ \rho v V + p\eta_y \\ (e+p)V - p\eta_t \end{Bmatrix} \qquad \tilde{H} = J^{-1}\begin{Bmatrix} 0 \\ 0 \\ -p/R \\ 0 \end{Bmatrix} \tag{9}$$

Here, R is the radial position from the centerline. The definition of the various terms in the axisymmetric equations are similar to their meaning in the 3-D case. Most important differences occur in the definition of the transformation metrics and Jacobian. The interested reader is referred to Refs. [3] and [4] for the expressions of the Jacobian and the metrics. We further emphasize that the centerline is a singularity of the transformation in the axisymmetric case.

NUMERICAL IMPLEMENTATION AND BOUNDARY CONDITIONS

The governing equations were implemented through the use of finite difference methods. The implicit Euler method was used for the time-march, and the spatial derivatives were approximated by three-point, second order central differences. The Beam and Warming implicit approximate factorization scheme[1, 2] was used for the solution of the resulting finite difference equations in order to obtain a cost efficient algorithm. The factored finite difference equations can be written in the delta form as

$$L_\eta L_\zeta L_\xi \Delta_t \overline{Q}^n = R_\xi + R_\eta + R_\zeta \tag{10}$$

The various operators are defined as

$$
\begin{aligned}
L_\xi &= I + \Delta t \delta_\xi \hat{A}^n - \epsilon_I \Delta t J^{-1} \nabla_\xi \Delta_\xi J & R_\xi &= -\Delta t \delta_\xi \overline{E}^n - \epsilon_E \Delta t J^{-1} (\nabla_\xi \Delta_\xi)^2 J \overline{Q}^n \\
L_\eta &= I + \Delta t \delta_\eta \hat{B}^n - \epsilon_I \Delta t J^{-1} \nabla_\eta \Delta_\eta J & R_\eta &= -\Delta t \delta_\eta \overline{F}^n - \epsilon_E \Delta t J^{-1} (\nabla_\eta \Delta_\eta)^2 J \overline{Q}^n \\
L_\zeta &= I + \Delta t \delta_\zeta \hat{C}^n - \epsilon_I \Delta t J^{-1} \nabla_\zeta \Delta_\zeta J & R_\zeta &= -\Delta t \delta_\zeta \overline{G}^n - \epsilon_E \Delta t J^{-1} (\nabla_\zeta \Delta_\zeta)^2 J \overline{Q}^n
\end{aligned} \tag{11}
$$

In the above, δ_ξ, δ_η and δ_ζ are central difference operators; ∇_ξ, ∇_η and ∇_ζ are backward difference operators; and Δ_ξ, Δ_η and Δ_ζ are forward difference operators in the ξ- , η- and ζ-directions, respectively. The Δ_t is a forward difference operator in time given by

$$
\Delta_t \overline{Q}^n = \overline{Q}^{n+1} - \overline{Q}^n \tag{12}
$$

Artificial dissipation terms have been introduced in the operators described by Eq. (11) in order to maintain the stability of the numerical solution process. Fourth order numerical dissipation terms were added to the right-hand side operators, and second order terms were used in the left-hand side operators. The Jacobian matrices $\hat{A}^n$, $\hat{B}^n$, $\hat{C}^n$, $\hat{M}_\xi^n$, $\hat{M}_\eta^n$ and $\hat{M}_\zeta^n$ are described in detail in Refs. [7] and [8].

The implementation of the axisymmetric formulation follows precisely the same lines as described above for the 3-D case, since the Beam and Warming algorithm was also used for the solution. We will not repeat the details of this implementation for the sake of brevity, except to mention that the source term was treated fully explicitly in the present case. The same form of the artificial dissipation terms used in the 3-D case are also implemented in the axisymmetric code. This was helpful in order to use the axisymmetric code to estimate the sensitivity of the present 3-D results to variations in the artificial dissipation coefficients.

At the far field boundaries, both upstream and lateral, freestream conditions were assumed. The downstream boundary was treated according to one dimensional characteristic relations[10], which automatically provide the appropriate consideration of subsonic or supersonic outflow. Flow tangency conditions are enforced at the body wall. All of these boundary conditions were used both in the 3-D and axisymmetric formulations. In the 3-D case, pressure at the body wall is obtained by assuming a zero normal pressure gradient condition. The same condition is used in the axisymmetric case, except that a centrifugal force correction[11, 12] is added on the spherical nose region.

The major boundary condition differences between the 3-D and axisymmetric cases occur at the upstream centerline. In the 3-D case, properties at the centerline are obtained by linear extrapolation of the property values at the two adjacent points along the corresponding ξ-line, together with averaging in the ζ-direction which ensures consistency with the fact that a computational ζ-line is actually a single physical point along the centerline. In the axisymmetric case, since the radius R goes to zero at the centerline, we avoided defining a computational line exactly along the upstream centerline. Hence, a symmetry condition about the centerline is enforced defining another computational line which is symmetric to the last interior grid line. Finally, some boundary condition must be specified for the ζ, or circumferential, direction. In the present case, periodic boundary conditions were used in this direction.

RESULTS AND VALIDATION

The computational meshes used in the present work were generated by algebraic methods. A typical longitudinal plane of the grid is shown in Fig. 1. The particular mesh shown has 45 × 30 points in the longitudinal plane, and 26 points in the circumferential direction (not shown). Details of the forebody region are shown in Fig. 2. Care was exercised in order to ensure grid orthogonality at the forebody conical section. This was accomplished in the present case by the use of appropriate variable order polynomial grid generation functions[3]. Moreover, the grid stretching in the normal direction is also evident in both figures. We emphasize that the configuration considered in the present work is composed of a spherical nose, a conical section, and a cylindrical afterbody.

Pressure coefficient distributions along the body for a $M_\infty = 1.527$ and zero angle of attack are shown in Fig. 3. The 3-D computational mesh used for these calculations has 45 × 30 × 26 grid points. Three dimensional results are compared with the axisymmetric computations, and it is clear from the figure that the pressure distributions are in good agreement. The axisymmetric results presented in Fig. 3 were obtained using the same longitudinal grid plane employed in the 3-D computations, and the same levels of artificial dissipation coefficients. The major differences between the two computations occur at the spherical nose region, near the centerline stagnation point. These differences can be attributed to the rather different form in which the upstream centerline numerical boundary condition is enforced in the two codes. Moreover, as previously discussed, there also are differences in the implementation of the wall pressure boundary condition at the spherical nose region between the two codes. The stagnation point pressure coefficient for the 3-D computation is in much better agreement than the 2-D one with the stagnation C_p which would be obtained at that point by simple isentropic and normal shock relations. Results for a $M_\infty = 2.55$ case, still at zero angle of attack, are shown in Fig. 4. As in the previous case, three dimensional computations are compared to axisymmetric calculations, and similar observations could be made with respect to the results obtained.

Pressure coefficient distributions for $M_\infty = 1.527$, and $\alpha = 5°$, are shown in Fig. 5 for a few circumferential grid planes. Although we do not have any results with which to compare these computations, it is clear from Fig. 5 that the calculations are presenting the expected behavior. We observe that all computations presented in Figs. 3, 4 and 5 were performed using the same levels of artificial dissipation coefficients, including the axisymmetric runs. Similar comparisons were obtained for a $M_\infty = 2.55$ flight case with $\alpha = 5°$. For both Mach numbers, computations for a

$\alpha = 3°$ case were also performed. These results are not shown here due to the present space limitations, and because the conclusions that can be drawn are essentially equivalent to the ones obtained from the previous figures.

The computations performed for this configuration considered three grid sizes in an attempt to study the effect of grid refinement in the solutions. Fig. 6 presents the effect of this refinement on the body pressure coefficient distribution for a three dimensional computation at $M_\infty = 1.527$ and $\alpha = 0°$. The meshes used had $33 \times 20 \times 20$ and $45 \times 30 \times 26$ points for the coarse and medium meshes, respectively. The current medium size mesh was the largest grid we used for 3-D calculations for this configuration, in order to avoid excessive computational costs. It is clear from Fig. 6 that there is considerable difference between the results for the coarse and medium grids in this case. The comparison of results at angle of attack for the coarse and medium grids is shown in Fig. 7. Here, a $M_\infty = 2.55$ and $\alpha = 3°$ case is considered, and the figure compares leeside pressure coefficient distributions. Despite some differences at the sphere-cone junction, the results in this case are in much better agreement. This trend is typical of the computational results obtained in the present investigation, in the sense that the differences in the body pressures are more relevant at the $M_\infty = 1.527$ case than at the $M_\infty = 2.55$ case.

Further grid refinement studies were performed using the axisymmetric code. A typical result is shown in Fig. 8, where the computations for the $M_\infty = 1.527$ case are shown. In this case, we are comparing the results for a 67×45 point mesh with those for a 45×30 mesh. We will be referring to these as the fine and medium meshes, respectively. We observe that the two results are in good agreement, except for some differences at the sphere-cone junction expansion peak. This result indicates that, as far as mesh independence is concerned, the medium size grid already gives engineering accuracy for a preliminary analysis, even for the $M_\infty = 1.527$ case. As previously discussed, the differences are more relevant at this lower supersonic Mach number than at higher Mach numbers.

A study of the effect of the artificial dissipation coefficients was performed with the objective of quantifying their influence in the final solutions. Fig. 9 presents the pressure coefficient distributions for the axisymmetric computations at a freestream Mach number $M_\infty = 1.527$ with three different levels of artificial dissipation. The curves show results for $\epsilon_E = 5$, 10 and 20. For all cases, we used $\epsilon_I = 3\epsilon_E$. The major concern in the present work was that all 3-D computations have used $\epsilon_E = 20$. This is about one order of magnitude higher than what is usually recommended in the literature[7] and, therefore, it is necessary to quantify the effect that such high values of artificial dissipation coefficients could have in the accuracy of the results. It is clear from Fig. 9 that the influence is small over most of the body, but there is a definite tendency of flattening the expansion peaks as the magnitude of the artificial dissipation coefficients is increased. At least for the applications here, these differences are within acceptable engineering safety margins. However, one should be aware that the influence of these numerical parameters may not be negligible.

Finally, in order to have at least some comparison with experimental results, one case considering the VLS geometry was run. For a description of the VLS vehicle, the interested reader is referred to the work of Moraes and Neto[5], and Moraes et al.[13]. In the present case, we considered the 2nd stage flight configuration, and assumed $M_\infty = 1.5$ and $\alpha = 4°$. The computational mesh was also generated by algebraic methods, as the previous grids. Fig. 10 presents lee- and windside pressure coefficient distributions obtained by the present computation as compared to experimental results. We observe that only the vehicle forebody results are shown in this figure, and that the mesh used has $63 \times 34 \times 26$ points. The agreement with experiment is certainly not perfect, but the present computations are capturing the correct trend. The most significant differences, occur at the boattail region, $0.15 \leq x/L \leq 0.20$, and at the cylindrical afterbody. The reasons for the discrepancies observed are currently being investigated.

CONCLUDING REMARKS

The development of a three dimensional Euler solver based on finite difference methods has been described. The code was constructed envisioning mostly the aerodynamic design of general launch vehicle configurations. Some partial validation of the three dimensional code was possible using an available axisymmetric code which had previously been tested against experimental results. Grid refinement studies and studies of the sensitivity to some computational parameters were performed with the objective of increasing the confidence in the code developed. Moreover, these studies also have the objective of quantifying the influence of these features in the accuracy of the results. Comparison of the code results to experimental data has shown that there is still need for further validation.

To give an idea of the computational costs involved, 3-D calculations for the $45 \times 30 \times 26$ mesh take of the order of 10.5 CPU seconds per iteration in a Convex C-210. Convergence usually requires between 2500 to 3500 iterations for three orders of magnitude drop in the residue. The axisymmetric computations reported here were performed in smaller equipment. Calculations with the 45×30 mesh use about 28 CPU seconds per iteration in a Definicon DSI-020 board. The same mesh would require 0.9 seconds per iteration in the Convex. In the axisymmetric case, convergence is usually achieved around 3000 iterations, again with three orders of magnitude drop in the residue.

It should be emphasized that only supersonic flight conditions were considered in the present effort because, for the vehicle under consideration, dimensioning structural loads occur in this flight regime. The two freestream Mach numbers considered for the these computations correspond to maximum vehicle bending moment at the nose fairing attachment point and to the maximum dynamic pressure condition. However, it would be very interesting to study the code behavior in the transonic flight regime, because this is usually a more stringent condition for the validation of flow simulation codes. At present, the efforts as a continuation of this work are directed towards improving the computational efficiency of the code by the use of a few convergence acceleration techniques. The use of alternate numerical solution algorithms and the implementation of zonal techniques are also currently under consideration.

REFERENCES

[1] R.M. Beam and R.F. Warming, J. Comput. Phys. **22**, 87 (1976).

[2] R.M. Beam and R.F. Warming, AIAA J. **16**, 393 (1978).

[3] F. Zdravistch, "Aerodynamic Flow Simulation Over Cluster Type Configurations," Master Thesis, Instituto Tecnológico de Aeronáutica, São José dos Campos, SP, Brazil, Nov. 1990 (in Portuguese, original title is "Simulação de Escoamentos Aerodinâmicos em Configurações Tipo Cluster").

[4] F. Zdravistch and J.L.F. Azevedo, "Numerical Simulation of High Speed Flows Over Complex Satellite Launchers," *Proceedings of the 3rd Brazilian Thermal Sciences Meeting*, Vol. I, Dec. 1990, pp. 233-238.

[5] P. Moraes Jr. and A.A. Neto, "Aerodynamic Experimental Investigation of the Brazilian Satellite Launch Vehicle (VLS)," *Proceedings of the 3rd Brazilian Thermal Sciences Meeting*, Vol. I, Dec. 1990, pp. 211-215.

[6] T.H. Pulliam and J.L. Steger, AIAA J. **18**, 159 (1980).

[7] T.H. Pulliam and J.L. Steger, "Recent Improvements in Efficiency, Accuracy and Convergence for Implicit Approximate Factorization Algorithms," AIAA Paper 85-0360, Jan. 1985.

[8] J.L.F. Azevedo, "Transonic Aeroelastic Analysis of Launch Vehicle Configurations," NASA CR 4186, 1988.

[9] C.J. Nietubicz, T.H. Pulliam, and J.L. Steger, "Numerical Solution of the Azimuthal-Invariant Thin-Layer Navier-Stokes Equations," AIAA Paper 79-0010, Jan. 1979.

[10] J.L.F. Azevedo, "Euler Solutions of Transonic Nozzle Flows," *Proceedings of the 3rd Brazilian Thermal Sciences Meeting*, Vol. I, Itapema, SC, Brazil, Dec. 1990, pp. 243-248.

[11] R.W. MacCormack, "An Introduction and Review of the Basics of Computational Fluid Dynamics," AIAA Professional Study Series on Computational Fluid Dynamics, Snowmass, Colorado, June 1984.

[12] R.W. MacCormack, "Current Status of Numerical Solutions of the Navier-Stokes Equations," AIAA Paper 85-0032, Jan. 1985.

[13] P. Moraes Jr., F. Zdravistch, and J.L.F. Azevedo, "Aerodynamics of the Brazilian Satellite Launch Vehicle (VLS) During First Stage Separation," AIAA Paper 90-3098, *AIAA 8th Applied Aerodynamics Conference*, Aug. 1990.

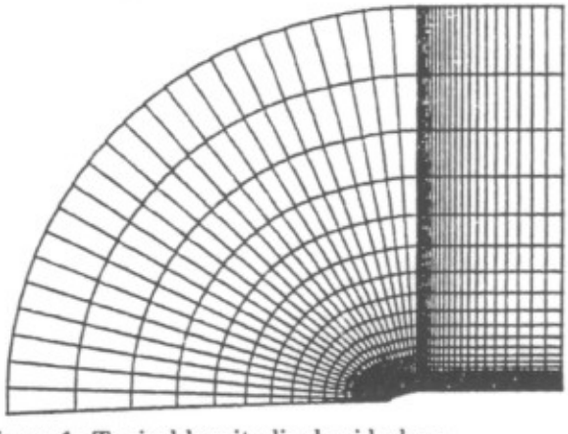

Figure 1: Typical longitudinal grid plane.

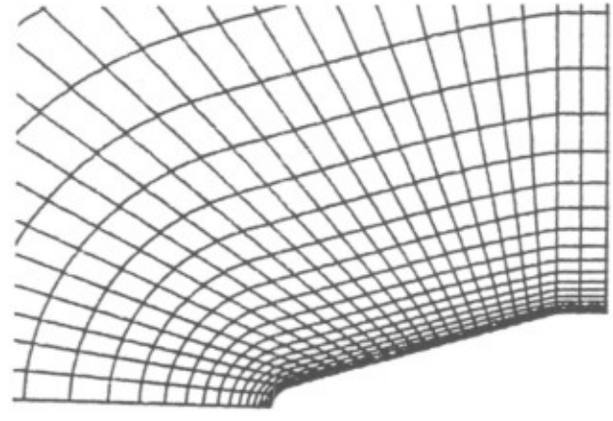

Figure 2: Detail of the grid in the forebody region.

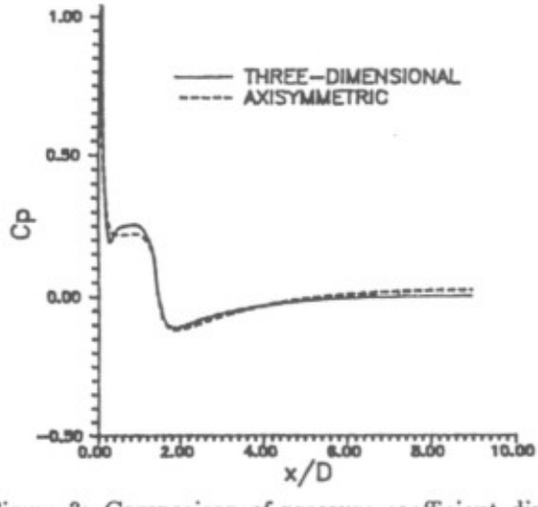

Figure 3: Comparison of pressure coefficient distributions over the body for $\alpha = 0°$ case ($M_\infty = 1.527$).

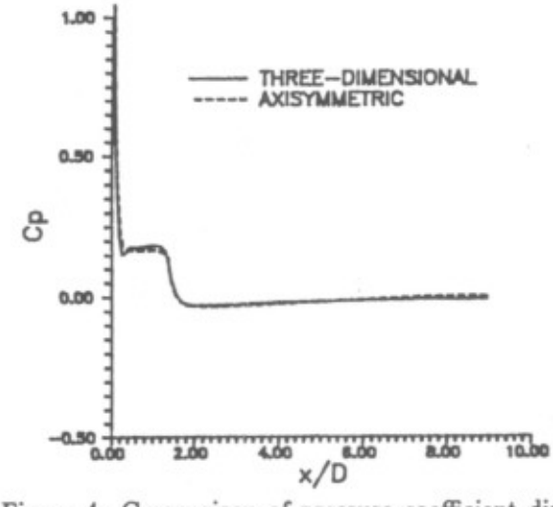

Figure 4: Comparison of pressure coefficient distributions over the body for $\alpha = 0°$ case ($M_\infty = 2.55$).

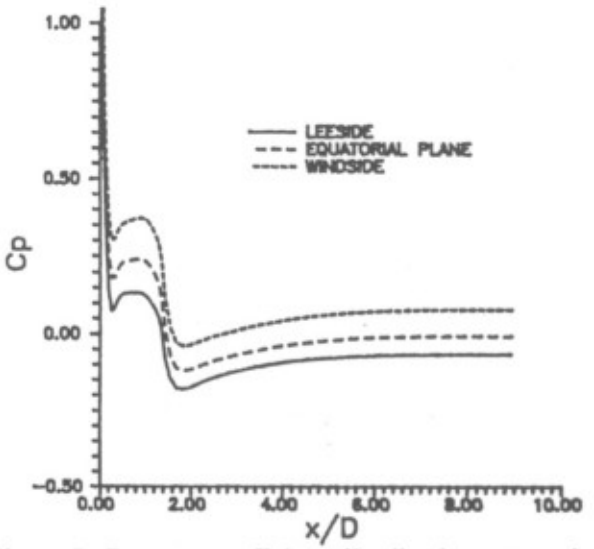

Figure 5: Pressure coefficient distributions at angle of attack ($M_\infty = 1.527$, $\alpha = 5°$).

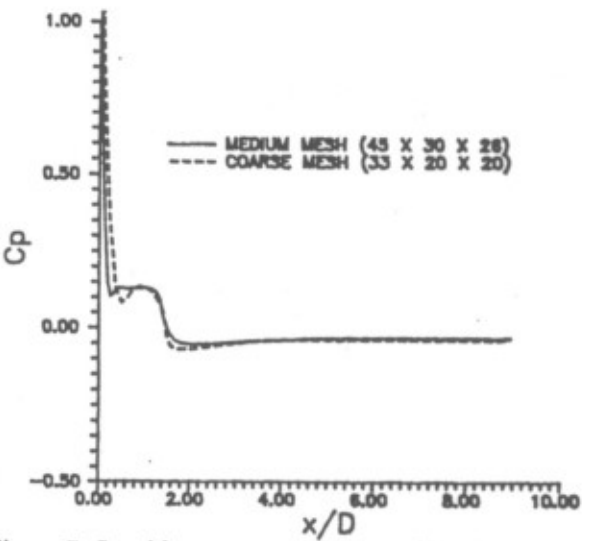

Figure 7: Leeside pressure coefficient distributions at $M_\infty = 2.55$ and $\alpha = 3°$.

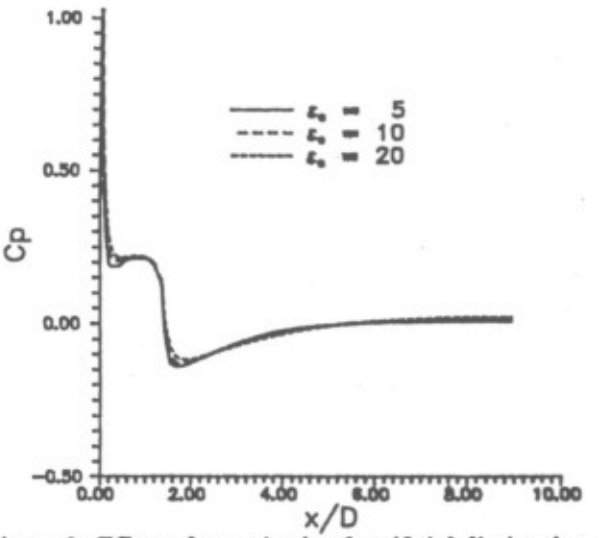

Figure 9: Effect of magnitude of artificial dissipation coefficients ($M_\infty = 1.527$, axisymmetric computation, $\epsilon_I = 3\epsilon_E$).

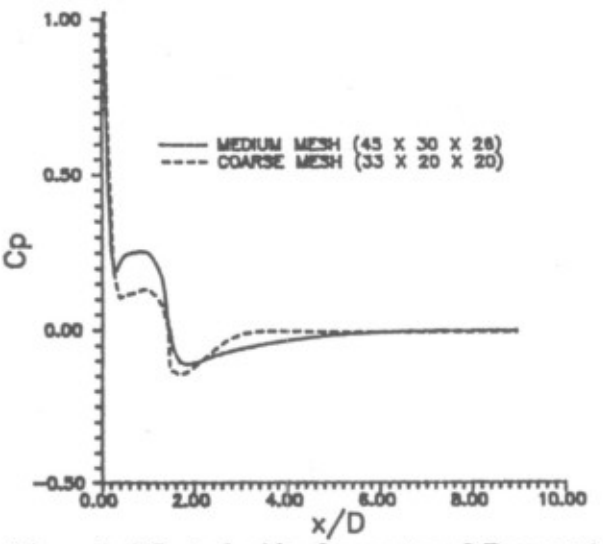

Figure 6: Effect of grid refinement on 3-D computations ($M_\infty = 1.527$, $\alpha = 0°$).

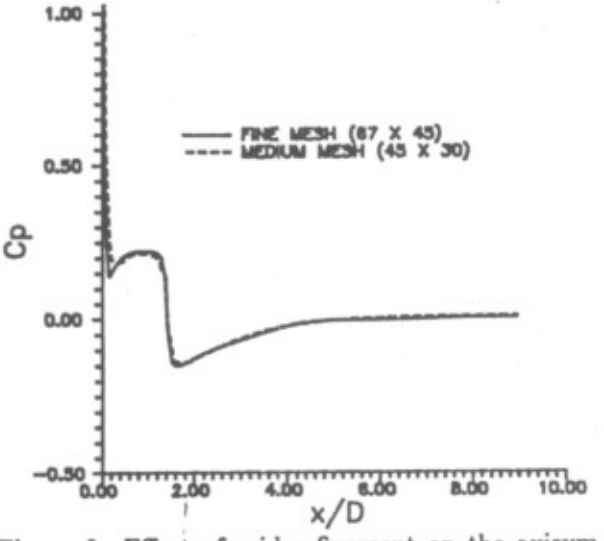

Figure 8: Effect of grid refinement on the axisymmetric calculations ($M_\infty = 1.527$).

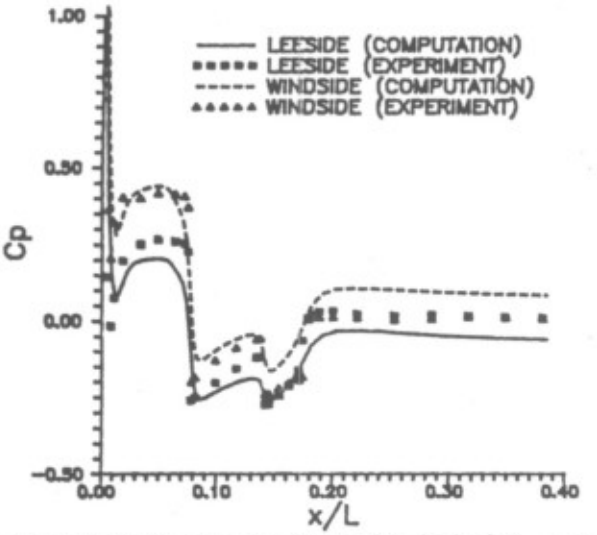

Figure 10: Results for the VLS vehicle ($M_\infty = 1.5$, $\alpha = 4°$).